Experimental assessment of ductile damage in P91 steel at high temperature

Guido Chiantoni[1], Claudia Comi[2], Stefano Mariani[2] and Nicola Bonora[3]

Introduction

Ductile failure is microscopically caused by the nucleation and growth up to coalescence of voids induced by large deformations. During a generic loading process, plastic deformations grow and a situation can be reached where at the macroscopic level the material can be still considered as a continuum, while at the microscale it consists of a matrix, inclusions, voids and cracks. Continuum damage mechanics can effectively describe the inelastic behavior of metallic alloys due to the presence and the growth of voids in a ductile matrix (see, e.g. Bonora et al., 2005; Brunig, 2003; Lemaitre, 1985a,b; Saanouni and Chaboche, 2003; Saanouni et al., 1994). The changes of the

[1]Dalmine S.p.A., Tenaris Dalmine R&D, Dalmine, Italy
[2]Dipartimento di Ingegneria Civile e Ambientale, Politecnico di Milano, Milano, Italy
[3]Dipartimento di Ingegneria Civile e Meccanica, Università degli Studi di Cassino e del Lazio Meridionale, Cassino, Italy

Corresponding author:
Stefano Mariani, Dipartimento di Ingegneria Civile e Ambientale, *Politecnico di Milano*, Piazza L. da Vinci 32, 20133 Milano, Italy.
Email: stefano.mariani@polimi.it

mechanical properties, in particular of the elastic moduli, are indicative of material degradation and their measurement can be used to determine appropriate damage indices.

As detailed in Lemaitre and Dufailly (1987), several direct and non-direct, or indirect methods can be adopted to this purpose (see also, Abed et al., 2012). The direct measurement methodology is based on micrographs taken after a cutting and polishing preparation of the samples. With this methodology, in Tinet et al. (2004), the damage in specimens, previously subject to tensile tests at high temperature, was measured by observing the voids with an optical microscope. However, this technique has several drawbacks since the cutting and polishing phases can locally plasticize the material, thus altering the damage distribution in the sample; furthermore, it allows to measure damage only at a given cut. Indirect measurements of damage in metals are instead based on the elastic modulus reduction under tensile tests with unloading and have been performed by various authors (see, e.g. Alves, 2001; Celentano and Chaboche, 2007; Spitzig et al., 1988). This technique is hardly applicable to testing conditions featuring very high temperatures, as strain gauges cannot be used in a furnace. A non-destructive technique, based on ultrasonic laser excitation at high temperatures, was developed in Nadal et al. (2009) to measure the shear modulus, but this technique is limited to the analysis of the specimen surface. In Thuillier et al. (2012), X-ray micro-tomography was used to measure the void volume fraction in notched aluminum alloy samples subject to tensile tests at room temperature.

In this work, we propose a comparative assessment of two alternative, indirect experimental techniques: the X-ray micro-tomography and the ultrasonic wave propagation. Both techniques are employed to determine the damage induced in the ferritic-martensitic steel ASTM A 335 grade P91 (hereinafter P91) by high temperature in either quasi-static or high strain rate tensile tests. Typical industrial applications of the P91 steel are ultrasupercritical boilers for the production of water steam and steam turbines for large-scale supply of electrical energy. In both cases, high efficiency is obtained by raising the operating conditions, in terms of pressure and temperature, up to about 300 bar and 600°C, respectively. During the industrial piercing and rolling processes, the material is deformed at high temperature (1100–1250°C); the resulting large plastic deformation can then produce plastic damage.

To investigate the material behavior in the harsh conditions mentioned here above, we performed uniaxial tensile tests on notched specimen at 1100°C and either low or high strain rates. In these tests, the void formation is accompanied by large viscoplastic strains and creep effects are present; in ductile material at high temperature conditions, creep damage could also be obtained by the measure of the tertiary strain rate in creep tests. In this work, to study the development of ductile damage, leading to the final failure of the specimens, two series of tests were performed up to different maximum values of nominal longitudinal strain. For all the tested specimens, the damage value, defined as the area of voids over the initial area, was measured by the micro-tomographic technique. An independent measurement of the mechanical properties degradation was then obtained by the ultrasonic wave propagation technique; in this latter case, in order to obtain a damage value from the variation of the longitudinal wave speed with respect to the virgin state, a micro-mechanical analysis was also developed. The damage estimates obtained with the two approaches are here compared.

Experimental procedure

Material

The 9% Cr–1% Mo steel grade P91 has a very high resistance to corrosion at high temperature and a low tendency to creep degradation. Its chemical composition, according to ASTM A335/A335M (2011) is reported in Table 1.

Table 1. Chemical composition of P91 steel, according to ASTM A 335 (mass percent).

	C	Mn	Si	P	S	Cr	Mo	V	Nb	N	Ni
Min	0.08	0.3	0.2	–	–	8.0	0.85	0.18	0.06	0.03	–
Max	0.12	0.6	0.5	0.02	0.01	9.5	1.05	0.25	0.1	0.07	0.4

The high percentage of chromium (about 9%) and molybdenum (about 1%) confers to the material high strength and improves the behavior in aggressive corrosion environments. The carbon content is low, as this element tends, during cooling, to lower the temperature corresponding to the starting point of martensitic transformation; this could be in contrast to the requirement for the final microstructure to be tempered martensite, even in the case of moderate cooling rates. Moreover, a higher carbon percentage would induce the formation of coarse carbides, with a tendency to decrease the creep resistance of the material. The presence of niobium and vanadium leads to the formation of nitrides finely dispersed throughout the metallic matrix, which represent obstacles to the dislocation motions and to the sliding of the grain boundaries, conferring to the material its creep resistance property. The tempered martensitic microstructure is obtained by a normalization heat treatment, to solubilize all the nitrides and carbides and to let the austenitic grains to grow in size. The tempering is then performed, inducing all the carbides and nitrides to homogeneously precipitate inside the metallic matrix.

The characteristic grain size changes with temperature and strain conditions. In order to correctly interpret the tomographic and ultrasonic measurements performed after the tensile tests illustrated in the following sections, one should estimate the grain size of the tested specimens. In the case of steel, the standard way to measure the grain size is to polish the sample and etching it using an appropriate acid solution able to react with the grain boundaries. Here, the polishing phase was performed in several steps with diamond pastes of different granulometry, and each step was followed by washing in a alcoholic cleaning solution. The etching of the polished surface was then performed with a solution of picric acid, hydrochloric acid and ethanol (Vilella etch), in which the samples were immersed for about a minute.

Figure 1 shows the image by light microscopy of a metallographic section where the material is undeformed. An accurate measurement of the grain size was not possible, but a roughly estimate of about 200 μm can be obtained. Figure 2 shows instead a metallography of the plastically deformed area in the central part of the specimen, where the deformation produced finer grains induced by the hot deformation process. The estimated grain size exhibited in this region is about 20 μm.

High temperature notch tensile tests

Tensile tests were performed on notched specimens, using a general purpose MTS 810 Material Testing System equipped with a MTS 653 furnace with three electrical resistances. A MTS 409.83 temperature controller was able to heat the specimens at a maximum nominal temperature of 1400°C. Three S-type thermocouples were adopted to measure the temperature in a closed loop control system; the accuracy of this temperature control had been previously verified using a specimen instrumented with three S-type welded thermocouples, and the measured maximum difference between the furnace and specimen thermocouples amounted to 1°C, within the error of the electronic chain of a single thermocouple. The furnace was sealed with standard kaowool. The target temperature for testing of 1100°C was reached in about 30 min; 10 additional minutes were required to homogenize the temperature in the furnace. During the heating stage, the specimen was clamped

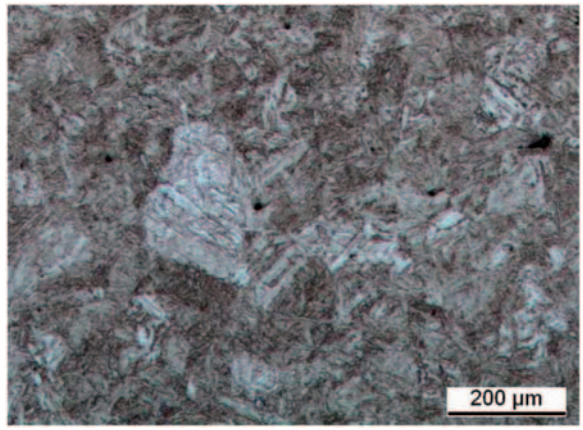

Figure 1. Microstructure of P91 specimen in an undeformed region (light microscopy).

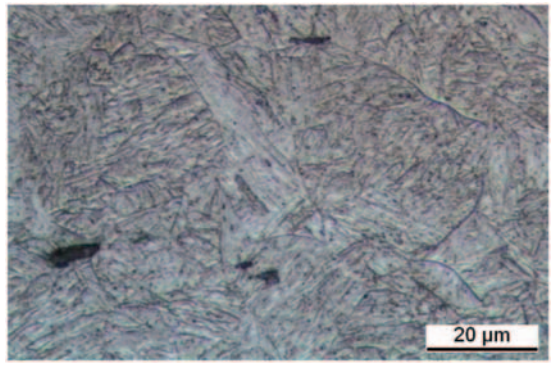

Figure 2. Microstructure of P91 specimen after hot deformation (light microscopy of a highly deformed region).

on the upper head only, while the lower one was kept free in order not to introduce an initial stress state due to thermal expansion.

The geometry of the notched specimen used for the tests is shown in Figure 3. The sample is particularly long to allow clamping outside the furnace. This experimental setup thus completely avoided all the difficulties caused by the deformation and loss of grip strength suffered by the clamping devices, when designed to operate inside the furnace.

After the heating stage, the specimen was clamped at the bottom head, and the test started. Two different velocities of the testing machine track were selected: 0.06 mm/s for the quasi-static tests and 50 mm/s for the high strain rate ones. For each velocity, four tests were carried out up to different values of the maximum imposed displacement of the moving track, and then interrupted in order to induce different damage levels inside the material. After the mechanical test, the specimens were immediately quenched in water. This operation took about 30 s and assured that the microstructure and the micro-voids formed at high temperature were correctly frozen.

The results obtained in terms of load versus displacement are shown in Figure 4 for the quasi-static case and in Figure 5 for the high strain rate case. It is worth noting that the load carrying

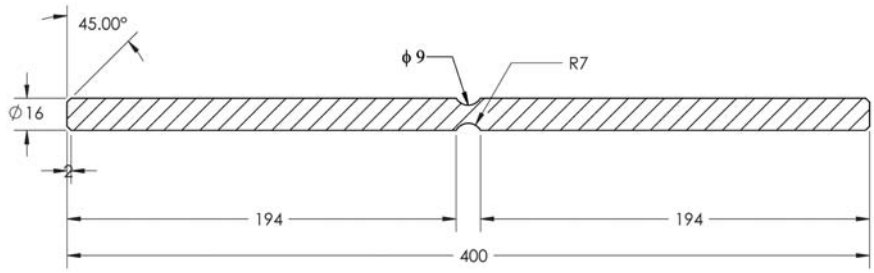

Figure 3. Geometry of the notched specimen (measures in mm).

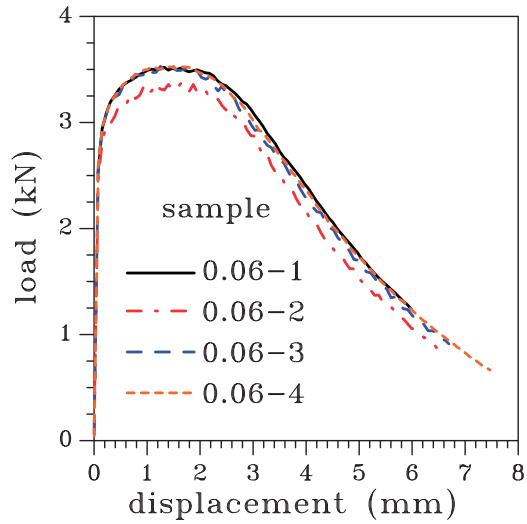

Figure 4. Quasi-static tensile tests, load vs. displacement curves.

capacity is more than doubled under high strain rate loading conditions. Despite the possible metallurgical variability among the different specimens, the spread obtained for tests interrupted at different maximum imposed displacements is very limited within each set of tests. The damage observed at the end of each test, even if experienced by different specimens, can be therefore considered as representative of the damage progressively developing in a single test up to failure.

Damage measurement

Micro-tomography

To measure the ductile damage cumulated in each specimen at the end of the tests, we first adopted a non-destructive technique based on three-dimensional (3D) images obtained by X-ray micro-tomography (micro-TAC). The measurements were performed in Grenoble (France) at the Novitom, using a synchrotron as a source of high-intensity X-rays, able to penetrate the metallic samples for tens of millimeters.

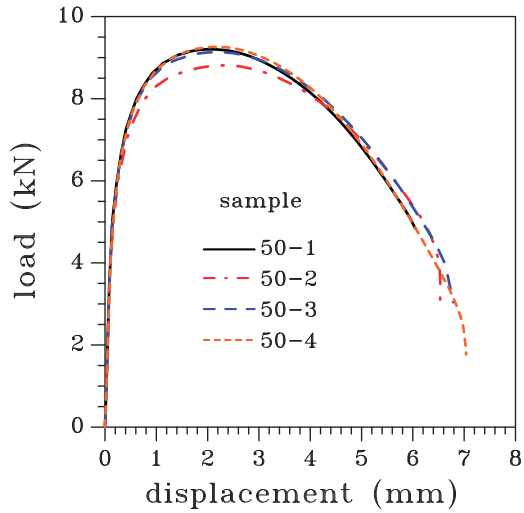

Figure 5. High strain rate tensile tests, load vs. displacement curves.

Micro-tomography must be performed at room temperature; to freeze the damage created with the high temperature testing, each specimen was rapidly quenched right after the end of the test, as described in "High temperature notch tensile tests" section. During this step, the lattice suffered an allotropic phase transformation creating martensitic laths. In order to verify that the thermal cycle did not induce micro-cracks, a specimen that underwent the thermal cycle only (including the final quenching) was examined through micro-tomography. Figure 6 shows a cross-section image of the specimen: no porosity or cracks were observed in all the sections, even when using the best possible resolution of 5 μm. It was then possible to conclude that the experimental protocol adopted for the post-test cooling of the specimens did not introduce any spurious damage.

The imaged volumes were 10 to 15 mm in diameter and 10 to 13 mm in height, taken from the central part of the tested specimens (labeled 0.06-1, 0.06-2, 0.06-3, 0.06-4 as for the quasi-static conditions and 50-1, 50-2, 50-3, 50-4 as for the high strain rate conditions). Images were taken every 0.01 mm along the sample longitudinal axes, showing the void content in the relevant cross sections; a high performance software, developed by Navitom, then enabled the 3D reconstruction of the entire sample from the slice images.

Figures 7 and 8 show the images in the necked regions of the samples tested under quasi-static and high strain rate loadings, respectively: the black spots indicate the micro-voids inside the sample. In the figures, the progressive necking of the region is accompanied by a decrease of the cross-section diameter (snapshots are all to scale). One can observe an obvious increase of damage or porosity with the maximum imposed displacement, and a significant localization in the central part of the section where stress triaxiality is higher (Needleman and Tvergaard, 1984). Even accounting for such localization of the porosity, under quasi-static loadings the induced voids keep rather dispersed in the cross section; on the contrary, under high strain rate loadings, the coalescence of the voids led to a macro-porosity formation clearly visible in Figure 8(d).

Figure 9 shows the 3D reconstruction of the sample 0.06-4. The micro-voids having an equivalent diameter (thought as an isotropic measure of their volume) greater than 15 μm are represented in blue. Once again, the damage appears to be localized in the central part of the necked region of the specimen.

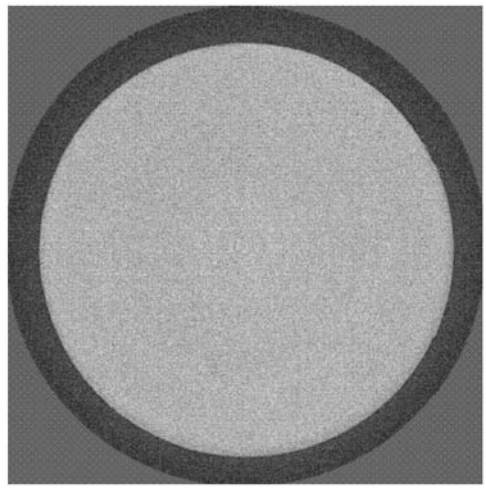

Figure 6. Micro-tomography of a P91 sample subjected to the thermal cycle only (maximum imposed displacement, MID = 0).

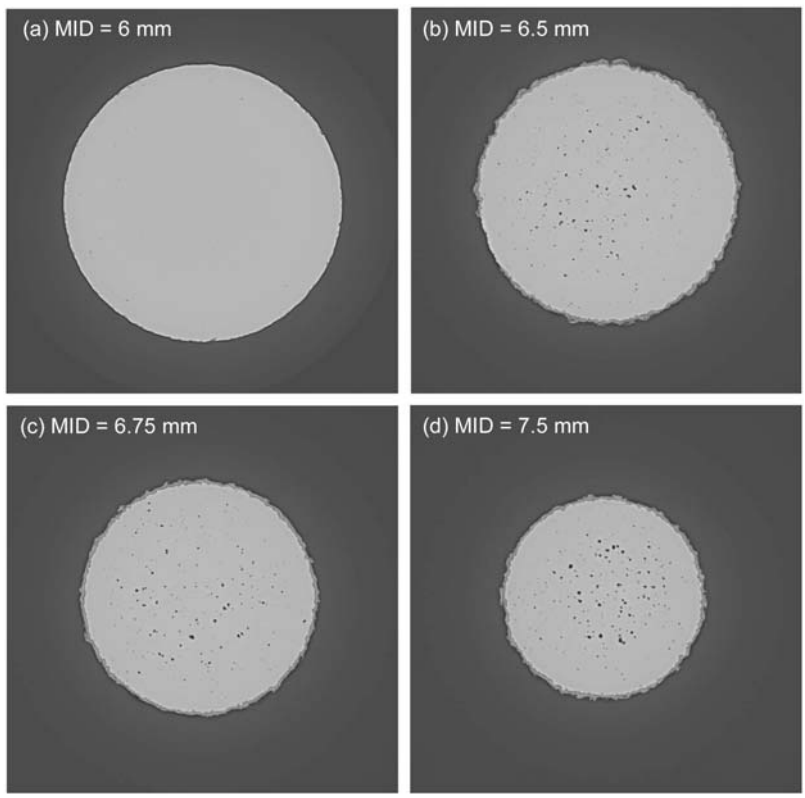

Figure 7. Quasi-static tensile tests, micro-tomographies of the necked cross sections of the specimens: (a) 0.06-1, (b) 0.06-2, (c) 0.06-3 and (d) 0.06-4. MID: maximum imposed displacement in mm.

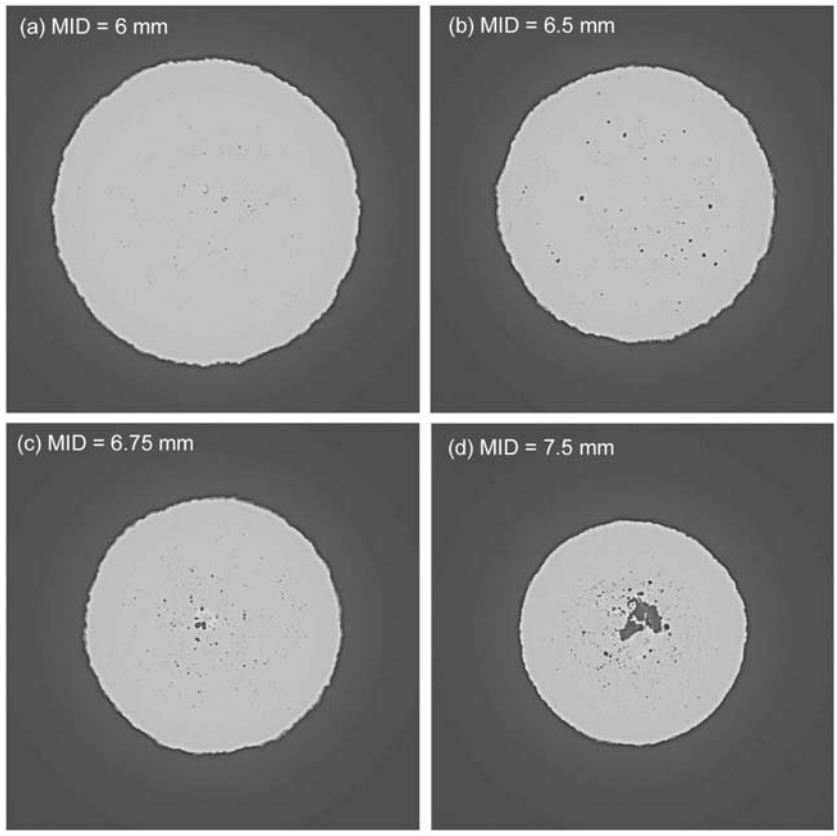

Figure 8. High strain rate tensile tests, micro-tomographies of the necked cross sections of the specimens: (a) 50-1, (b) 50-2, (c) 50-3 and (d) 50-4. MID: maximum imposed displacement in mm.

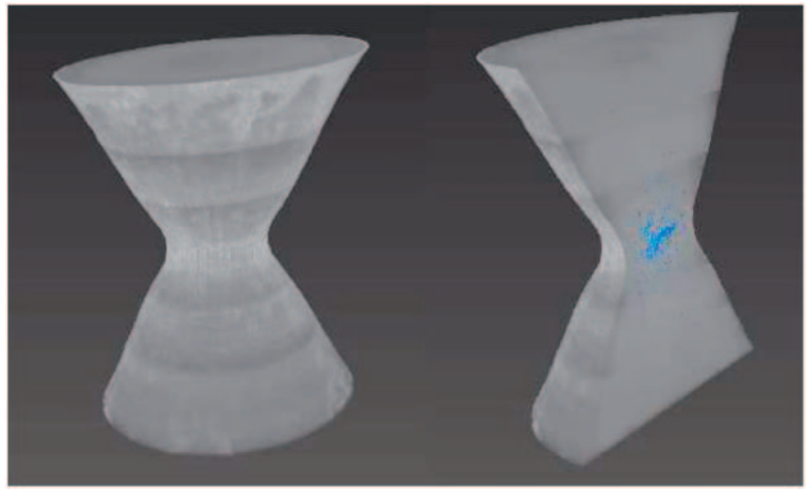

Figure 9. 3D reconstruction of sample 0.06-4, with microvoids represented in light blue.

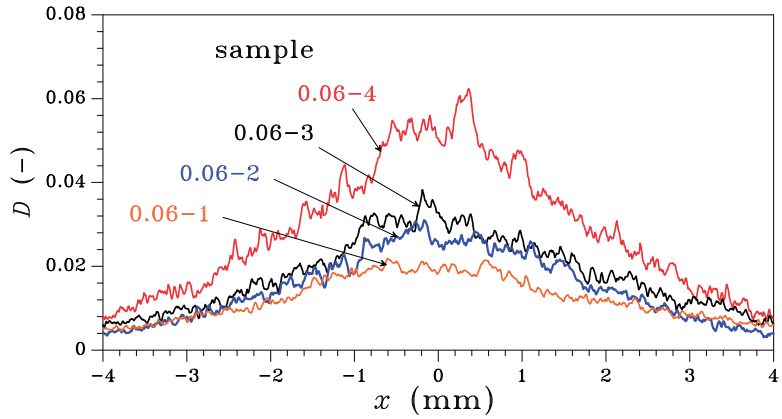

Figure 10. Quasi-static tensile tests, mean damage profiles along the axes of specimens (close-up of the central part only).

From all the images collected along the sample axis every 0.01 mm, one can obtain the mean value of damage over each cross section computed, according to classical damage mechanics, as the ratio between the area of the voids and the total cross-sectional area, namely:

$$D = \frac{A_{\text{voids}}}{A} \tag{1}$$

Since the 3D reconstruction showed that damage is always located in the core of a specimen, to avoid artifacts linked to the changing specimen diameter in the comparison with the outcomes of the ultrasonic measurements on the subsequently machined samples (see section "Ultrasonic method"), damage was computed through equation (1) using the area of the necked cross section as a measure of A.

The profiles of such smeared or cross-sectional damage along the sample axis are shown in Figures 10 and 11 for the quasi-static and high strain rate loadings, respectively. One can observe that the damage is more localized and features a higher peak value in the case of the high strain rate testing. Even though the damage values are here very low, one should notice that they actually represent smeared values over the specimen cross section, whose area is about 10mm^2; locally, in the center of the specimen over a representative volume element (RVE), values get much higher (see Figures 7 and 8). As discussed in "Material" section, the grain size in the deformed region is of about 20 μm; therefore, a reasonable RVE should feature a side length of 0.2 mm, so as the local value of damage can be computed over an area of about $(0.2\,\text{mm})^2$.

Ultrasonic method

The ultrasonic wave propagation methodology represents another indirect way to measure the decrease of the elastic properties.

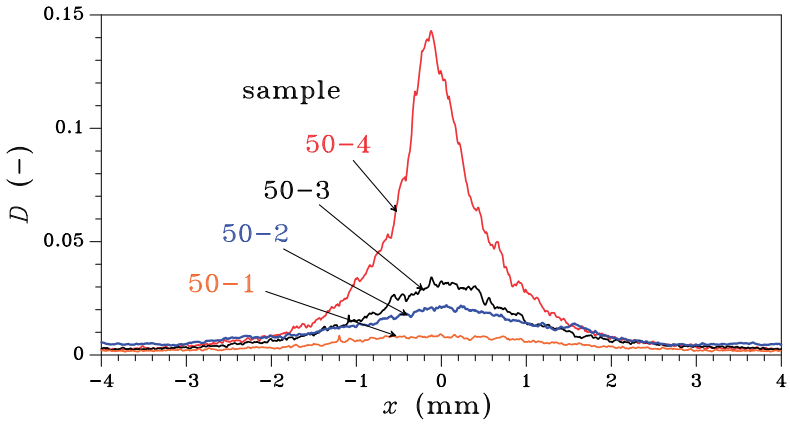

Figure 11. High strain rate tensile tests, mean damage profiles along the axes of specimens (close-up of the central part only).

In an isotropic elastic material, the velocities of propagation of longitudinal and shear waves respectively read:

$$v_L = \sqrt{\frac{\lambda}{\rho}} = \sqrt{\frac{E(1-\nu)}{\rho(1+\nu)(1-2\nu)}}$$
$$v_S = \sqrt{\frac{\mu}{\rho}} = \sqrt{\frac{E}{2\rho(1+\nu)}} \tag{2}$$

where λ and μ are the Lamé constants, E is the Young's modulus, ν is the Poisson's ratio and ρ is the material density. When damage occurs, the velocities of wave propagation decrease; from their measurement with some simplifying hypotheses on the microstructure evolution (see section "Micromechanical analysis"), one can compute the relevant damage levels.

Applications of this method, as available in the literature, are mainly devoted to quasi-brittle materials (see, e.g. Berthaud, 1991; Ohtsu, 2011). Here, we employ this methodology to measure ductile damage occurring in metals when tested at high temperature.

An important issue linked to the adopted ultrasonic wave speed technique is related to the accuracy of time interval measurement. This is a key aspect, as micro-tomography measurements reported very low damage values in the considered specimens; consequently, the expected variation due to damage of the wave time-of-flight is very small as well. The accuracy required to detect a given value of damage can be estimated using equation (2), and the ultrasonic wave reflection measurement relation $v_L = \frac{2t}{\tau}$ among the longitudinal wave velocity v_L, the specimen thickness t and the time-of-flight τ. Considering average elastic properties of the P91 steel ($E = 215$ GPa, $\nu = 0.28$), the time-of-flight τ of a longitudinal wave in a 4-mm-thick specimen is 1.36×10^{-6} s. The time shift corresponding to a damage value of 0.01 turns out to be of some nanoseconds. The used ultrasound digital pulser/receiver USPR-100 from MaGyc S.r.l. satisfies this sampling requirement, as it can measure time intervals as smaller as 10^{-9} s. This pulser was coupled with an Olympus XMS-310 – 10 MHz longitudinal ultrasound probe featuring 3 mm of external diameter. The probe is big enough to obtain a significant mean measurement, not affected by the grain boundaries; it is

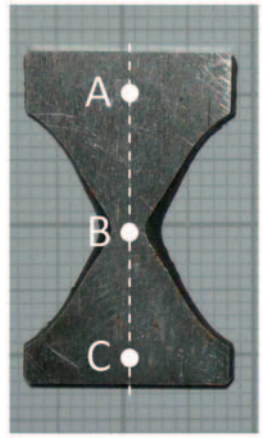

Figure 12. Location of points A, B and C along the longitudinal axis of any specimen tested with the ultrasonic technique.

also small enough, at least for the less deformed specimens (this point will be further discussed at the end of "Data reduction and comparative interpretation" section), in order not to introduce a strong noise in the echo signals, due to the reflections from the lateral surfaces of the samples in the necked area. A transverse probe Olympus V156 – 5 MHz was used to measure the shear wave velocity v_S and maintain the same signal resolution.

To accurately measure v_L, it is compulsory to minimize as much as possible the error of the thickness measurement for each sample. To get a uniform thickness t all over the region of interest, each deformed axisymmetric specimen was carefully milled to remove the edge material in the necked volume and obtain a flat sample with a thickness variation amounting to 0.01 mm at most. Figure 12 shows one sample, deformed under quasi-static conditions and so prepared for the ultrasonic measurements. To stabilize the sample temperature during the measurement and avoid any thermal expansion, the specimens were laid on a slab of granite that acted as a thermal reservoir at 20°C and stayed in contact with it for about 15 min before the test got started. The thickness t at any point of measurement was accurately determined with an error smaller than 1 μm; further to this, several repetitions of the test were done to reduce the error in the velocity calculation.

An ultrasonic test consisted of a series of measurements at the three points A, B and C along the specimen longitudinal axis, see Figure 12; at points A and C, the material is assumed to be undamaged (as confirmed by the tomographic observations like the one reported in Figure 9), while at point B in the necked region the material is surely damaged. A summary of the measured longitudinal wave speeds is given in Table 2. Using the estimated errors in the thickness and time-of-flight measurements, a standard error analysis provided a relative error on a single velocity measurement of about 0.4%, which has been lowered to less than 0.1% through the measurement repetitions.

The measurements in the undamaged regions (points A and C) gave longitudinal and shear velocity values of $v_L = 5929 \pm 15$ m/s and $v_S = 3278 \pm 12$ m/s. To assess the validity of the experimental procedure, we started from these values of the wave speeds in the undamaged regions to

Table 2. Measurements of the longitudinal wave speed v_L (in m/s).

Specimen	Maximum imposed displacement (mm)	Undamaged region		Damaged region
		Point A	Point C	Point B
0.06-1	6	5940.0	5950.6	5935.3
0.06-3	6.75	5937.2	5944.7	5865.5
0.06-4	7.5	5937.6	5934.8	5848.4
50-1	6	5909.3	5911.5	5915.9
50-2	6.5	5937.3	5932.1	5909.8
50-3	6.75	5930.9	5929.1	5892.5

compute the Poisson's ratio and the Young's modulus of the virgin material, by exploiting equation (2) according to:

$$\nu = \frac{v_L^2 - 2v_S^2}{2v_L^2 - 2v_S^2} = 0.28$$
$$E = \rho \frac{(1+\nu)(1-2\nu)}{(1-\nu)} v_L^2 = 216 \text{ GPa} \tag{3}$$

These values resulted to be in close agreement with those obtained by standard strain-gauge measurements, which amounted to $E = 215$ GPa and $\nu = 0.276$. The agreement between these values and those reported in equation (3) allows supporting the claim that the milling adopted to get flat specimens did not affect the material microstructure and, therefore, did not introduce further damage in the necked region.

To compute the damage value from the measure of the longitudinal wave speed in the damaged region (point B) of each specimen, one should consider that the nucleation and growth of the porosity reduce not only the elastic properties of the material, but also its density ρ. The micromechanical analysis (see next section) provides a way to establish all the required relations.

Micromechanical analysis

To assess the effects of damage on the speed of longitudinal waves in void-containing steel specimens, a micromechanical study is reported here. As for the notation, we mainly refer to Li and Wang (2008), where a thorough discussion on this topic is presented (see also, Nemat-Nasser and Hori, 1993). Hence, over-barred quantities stand for the overall properties of the damaged material, conceived as a two-phase (void and steel matrix) composite, whereas unbarred ones represent the properties of the virgin steel.

Denoting by f the porosity or void volume fraction, the density of the damaged material can be expressed by

$$\bar{\rho} = \rho(1-f) \tag{4}$$

To provide an analytical relationship between porosity and the overall elastic moduli, we frame the problem within the dilute dispersion approach, thereby neglecting any interaction among neighboring voids. A representative sample of the material is therefore assumed to consist of a spherical inhomogeneity, featuring null elastic stiffness, embedded into the steel matrix. Accordingly, the Eshelby tensor allows linking the overall bulk $\bar{K}$ and shear $\bar{\mu}$ elastic moduli to the relevant steel ones (K and μ) and to the void volume fraction f through:

$$\begin{aligned}\frac{\bar{K}^s}{K} &= \left(1+\frac{3(1-\nu)}{2(1-2\nu)}f\right)^{-1} \equiv \varphi_K^s \\ \frac{\bar{\mu}^s}{\mu} &= \left(1+\frac{15(1-\nu)}{7-5\nu}f\right)^{-1} \equiv \varphi_\mu^s\end{aligned} \tag{5}$$

in case of prescribed uniform stress boundary conditions, and through:

$$\begin{aligned}\frac{\bar{K}^e}{K} &= 1-\frac{3(1-\nu)}{2(1-2\nu)}f \equiv \varphi_K^e \\ \frac{\bar{\mu}^e}{\mu} &= 1-\frac{15(1-\nu)}{7-5\nu}f \equiv \varphi_\mu^e\end{aligned} \tag{6}$$

in case of prescribed uniform strain boundary conditions. Such expressions are functions of the void volume fraction f and of the steel Poisson's ratio ν only and provide rigorous upper and lower bounds on the actual overall properties of the void-containing steel, according to:

$$\begin{aligned}\bar{K}^e \le \bar{K} \le \bar{K}^s \\ \bar{\mu}^e \le \bar{\mu} \le \bar{\mu}^s\end{aligned} \tag{7}$$

Due to the assumed dilute dispersion of voids, estimates (5) and (6) do match up to the first order in f, if a Taylor series expansion of φ_K^s and φ_μ^s in (5) is computed.

We now aim to describe the effect of f on the overall Young's modulus $\bar{E}$, Poisson's ratio $\bar{\nu}$ and Lamé constant $\bar{\lambda}$ (see equation 2). According to the notation introduced in equations (5) and (6), the aforementioned elastic constants result to be bounded by:

$$\begin{aligned}\varphi_E^e E \equiv \bar{E}^e \le \bar{E} \le \bar{E}^s \equiv \varphi_E^s E \\ \varphi_\nu^e \nu \equiv \bar{\nu}^e \le \bar{\nu} \le \bar{\nu}^s \equiv \varphi_\nu^s \nu \\ \varphi_\lambda^e \lambda \equiv \bar{\lambda}^e \le \bar{\lambda} \le \bar{\lambda}^s \equiv \varphi_\lambda^s E\end{aligned} \tag{8}$$

where coefficients $\varphi_E^i, \varphi_\nu^i$ and φ_λ^i, $i=s$ or $i=e$, read:

$$\varphi_E^i = \frac{3\dfrac{K}{\mu}+1}{3\dfrac{K}{\mu}+\dfrac{\varphi_\mu^i}{\varphi_K^i}}\varphi_\mu^i$$

$$\varphi_\nu^i = \frac{3\dfrac{K}{\mu}+1}{3\dfrac{K}{\mu}+\dfrac{\varphi_\mu^i}{\varphi_K^i}}\frac{3\dfrac{K}{\mu}-2\dfrac{\varphi_\mu^i}{\varphi_K^i}}{3\dfrac{K}{\mu}-2}$$

$$\varphi_\lambda^i = \frac{\dfrac{K}{\mu}-\dfrac{2}{3}\dfrac{\varphi_\mu^i}{\varphi_K^i}}{\dfrac{K}{\mu}-\dfrac{2}{3}}\varphi_K^i \tag{9}$$

To provide a further measure of the effects of f on the elastic moduli, we refer to the self-consistent estimates of $\bar{K}$ and $\bar{\mu}$ which read (see Li and Wang, 2008):

$$\begin{aligned}\frac{\bar{K}^{s-c}}{K} &= 1-\frac{3(1-\bar{\nu}^{s-c})}{2(1-2\bar{\nu}^{s-c})}f \equiv \varphi_K^{s-c}\\ \frac{\bar{\mu}^{s-c}}{\mu} &= 1-\frac{15(1-\bar{\nu}^{s-c})}{7-5\bar{\nu}^{s-c}}f \equiv \varphi_\mu^{s-c}\end{aligned} \tag{10}$$

If compared to the lower bounds (6), the above estimates differ because of the presence of the overall Poisson's ratio $\bar{\nu}^{s-c}$ in place of the matrix one ν. Equations (10) are claimed to provide a nonlinear, implicit solution to the homogenization problem. Anyway, in the present case of a single spherical inclusion embedded into the steel matrix, the problem can be solved analytically by considering the ratio $\frac{\bar{K}^{s-c}/K}{\bar{\mu}^{s-c}/\mu}$, which turns out to be independent of the overall Young's modulus:

$$\frac{\dfrac{\bar{K}^{s-c}}{K}}{\dfrac{\bar{\mu}^{s-c}}{\mu}} = \frac{\dfrac{1+\bar{\nu}^{s-c}}{1+\nu}}{\dfrac{1-2\bar{\nu}^{s-c}}{1-2\nu}} = \frac{1-\dfrac{3(1-\bar{\nu}^{s-c})}{2(1-2\bar{\nu}^{s-c})}f}{1-\dfrac{15(1-\bar{\nu}^{s-c})}{7-5\bar{\nu}^{s-c}}f} \tag{11}$$

The physically sound solution to the second-order equation (11) in $\bar{\nu}^{s-c}$ is:

$$\bar{\nu}^{s-c} = \frac{7-6f+5\nu-6\nu f-\dfrac{1}{2}\sqrt{(-14+12f-10\nu+12\nu f)^2-4(3f+14\nu-27\nu f)(10-15f+15\nu f)}}{10-15f+15\nu f} \tag{12}$$

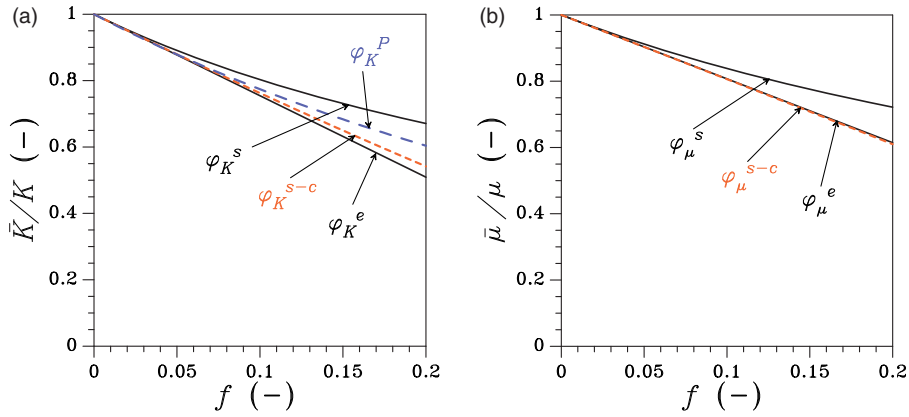

Figure 13. Effect of the void volume fraction f on the overall (a) bulk $\bar{K}$ and (b) shear $\bar{\mu}$ moduli of the void-containing steel.

which provides $\frac{\bar{\nu}^{s-c}}{\nu} \equiv \varphi_\nu^{s-c}$. This solution then allows to analytically estimate $\bar{K}^{s-c}$ and $\bar{\mu}^{s-c}$ through equations (10). $\bar{E}^{s-c}$ and $\bar{\lambda}^{s-c}$ are instead obtained, in perfect analogy with the former bounds, through:

$$\begin{aligned}
\frac{\bar{E}^{s-c}}{E} &= \frac{3\dfrac{K}{\mu}+1}{3\dfrac{K}{\mu}+\dfrac{\varphi_\mu^{s-c}}{\varphi_K^{s-c}}}\varphi_\mu^{s-c} \equiv \varphi_E^{s-c} \\
\frac{\bar{\lambda}^{s-c}}{\lambda} &= \frac{\dfrac{K}{\mu}-\dfrac{2}{3}\dfrac{\varphi_\mu^{s-c}}{\varphi_K^{s-c}}}{\dfrac{K}{\mu}-\dfrac{2}{3}}\varphi_K^{s-c} \equiv \varphi_\lambda^{s-c}
\end{aligned} \tag{13}$$

The effect of the void volume fraction f on the overall elastic moduli is now investigated in the case $\nu = 0.28$, of interest for the P91 steel (see section "Ultrasonic method"). Figure 13 shows the variation of $\bar{K}$ and $\bar{\mu}$ with f; according to the assumption of dilute dispersion of voids, results are reported only up to $f = 0.2$, which proves sufficient for the present investigation (see "Data reduction and comparative interpretation" section). Plots testify that the self-consistent approach provides an estimate for $\bar{K}$ close to the lower bound $\bar{K}^e$, while the estimate for $\bar{\mu}$ is practically indistinguishable from the lower bound. As a further term of comparison, Figure 13(a) also reports the periodic solution:

$$\frac{\bar{K}^P}{K} = 1 - \frac{3(1-\nu)}{2(1-2\nu)+(1+\nu)f}f \equiv \varphi_K^P \tag{14}$$

which is coincident with the Hashin–Shtrikman upper bound, see (Nemat-Nasser and Hori, 1993).

Results relevant to the overall $\bar{E}$, $\bar{\nu}$ and $\bar{\lambda}$ are instead reported in Figure 14. Figure 14(b) shows that the effect of f on $\bar{\nu}$ is marginal: even for $f = 0.2$, the overall Poisson's ratio gets reduced by about 10% only. Such reduction amounts to 2% at most, if f is within the range of interest for the data

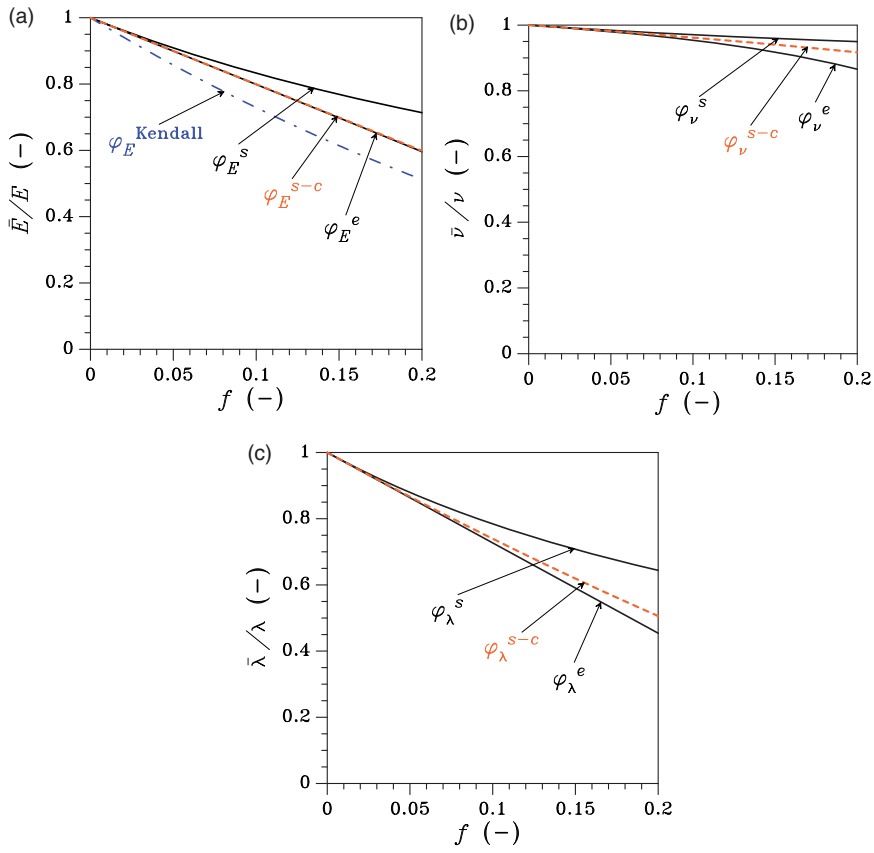

Figure 14. Effect of the void volume fraction f on the overall (a) Young's modulus $\bar{E}$, (b) Poisson's ratio $\bar{\nu}$ and (c) Lamé constant $\bar{\lambda}$ of the void-containing steel.

reported in "Data reduction and comparative interpretation" section, i.e. if $f \leq 0.05$. Since the solutions provided by bound (6) and by (12) are also very close to each other, the relevant descriptions of the effect of f on $\bar{E}$ practically match too. These outcomes provide a basis for the simplifying assumption, commonly done in damage mechanics, that ductile damage is isotropic and can be described by the single damage variable D, so that the current elastic properties of the damaged material can be given as:

$$\begin{aligned} \bar{E} &= E(1-D) \\ \bar{\nu} &= \nu \end{aligned} \tag{15}$$

Finally, as far as $\bar{E}$ is concerned, Figure 14(a) also shows the empirical interpolation provided in Kendall et al. (1983), on the basis of a former analysis given in Hansen (1965), which reads:

$$\frac{\bar{E}^{\text{Kendall}}}{E} = (1-f)^3 \equiv \varphi_E^{\text{Kendall}} \tag{16}$$

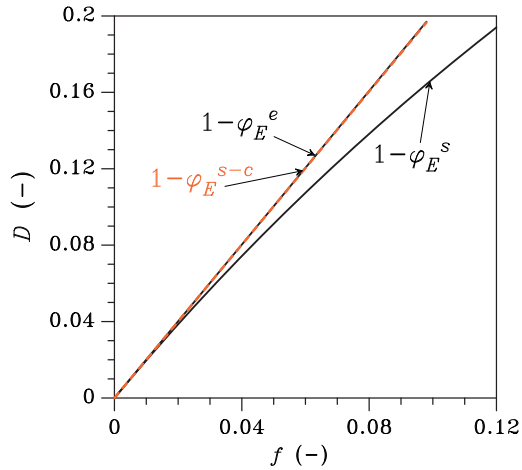

Figure 15. Upper and lower bounds and self-consistent estimation for the damage vs. porosity relationship, having assumed the Poisson's ratio to be independent of *D*.

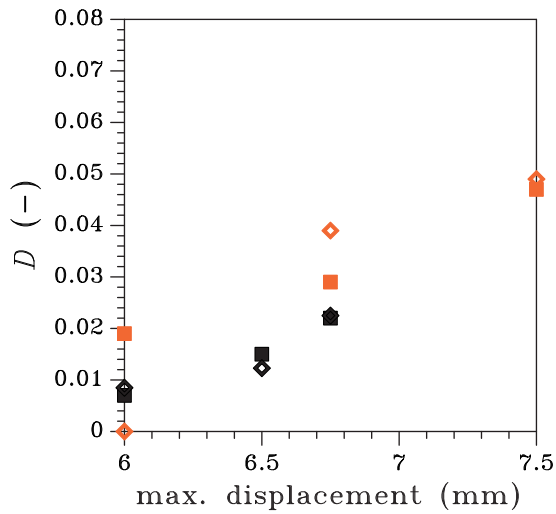

Figure 16. Comparison between damage values in the necked specimen regions, as obtained with micro-tomography (squares) and ultrasonic measurements (diamonds), at varying maximum imposed displacement during the tensile test. Quasi-static test results are reported in orange, whereas high strain rate test results are reported in black.

Even if sometime adopted to describe the impact of porosity on the overall Young's modulus (Comi et al., 2009; Heukamp et al., 2001), equation (16) overestimates the reduction of $\bar{E}$ for the range of f values of interest in the present work. Moreover, it is not compliant with the lower bound furnished by (6), (8) and (9); hence, it will not be considered in the comparative assessment of the two experimental techniques, to be provided next.

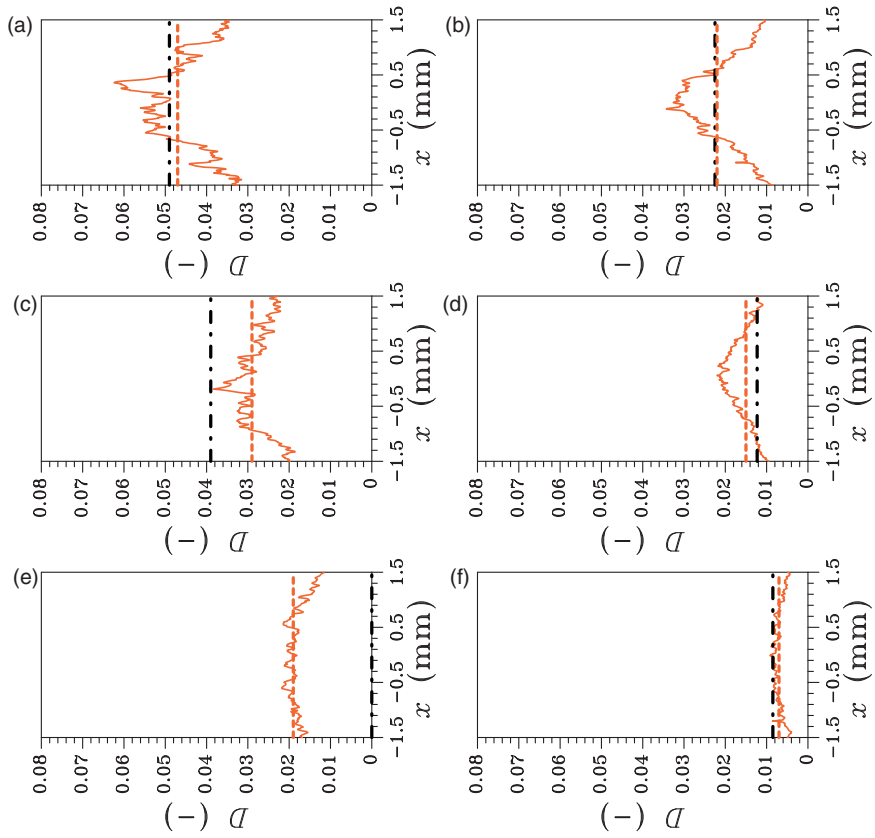

Figure 17. Comparison among cross-sectional damage profiles (orange continuous lines) and overall damage levels (orange dashed lines) given by micro-tomography, and overall damage levels (black dot-dashed lines) given by ultrasonic measurements. Left column: quasi-static tests; right column: high strain rate tests. From bottom to top, results are reported at increasing values of the maximum imposed track displacement on specimens: (a) 0.06-4, (b) 50-3, (c) 0.06-3, (d) 50-2, (e) 0.06-1 and (f) 50-1.

Data reduction and comparative interpretation

By assuming that damage does not (or does negligibly) affect the material Poisson's ratio, i.e. that $\bar{\nu} = \nu$ (see equation 15), equation $(2)_1$ can be exploited to link the longitudinal wave velocities v_L and $\bar{v}_L$ in the undamaged and damaged regions through:

$$\frac{\bar{v}_L^2}{v_L^2} = \frac{\bar{E}/\bar{\rho}}{E/\rho} \tag{17}$$

Using equations (8) and (4), relation (17) provides upper and lower bounds on the porosity f in the damaged region based on the measured $\frac{\bar{v}_L^2}{v_L^2}$ ratio. Recalling that damage is related to the Young's modulus reduction by $D = 1 - \frac{\bar{E}}{E}$, see again equation (15), one can finally obtain upper and lower bounds for D. Note that, as shown in Figure 15, for the range of values of porosity of interest here, the upper and lower bounds look much tight.

For each tested specimen, the value of $\bar{v}_L$, i.e. of the wave speed at point B, was taken from the measurements reported in Table 2; v_L was instead kept as the average value over all the tests, already reported in ''Ultrasonic method'' section. Damage values so obtained are shown in Figure 16 (diamond symbols) as a function of the maximum imposed track displacement. Here results are shown for the quasi-static case (orange symbols) and for the high strain rate case (black symbols); due to the small values of the cross-sectional damage, the upper and lower bounds are practically superposed within the chosen scale. As already noted, the measurements on specimens tested at the same displacement rate and up to different maximum imposed displacement values can be intended to provide an evolution of damage at increasing track displacement in a single tensile test.

The damage values in Figure 16 that are related to micro-tomography (square symbols) were computed from the profiles reported in Figures 10 and 11 as a weighted mean value over the central specimen region corresponding to the area of the ultrasonic probe. The values relevant to the ultrasonic wave propagation technique (diamond symbols) were instead obtained at point B, namely at the central necked cross section, through the data reduction procedure described here above. To get deeper insights into the proposed comparison, Figure 17 provides a close-up of the aforementioned damage profiles along the longitudinal axes of the specimens, with a focus on the region across the necked cross section ($x = 0$) of size 3 mm equal to the probe diameter. In these graphs, the profiles are plotted as orange continuous lines, while the dashed orange lines stand for the weighted averages in the region, which are not to be interpreted as homogeneous values along x but instead as overall D values to be compared with those furnished by the ultrasonic technique, represented by the black dot-dashed lines.

Despite some scattering, one can observe that the agreement between the two overall damage estimations is reasonably good, except for the sample 0.06-1. In such a case, the ultrasonic measurement of $\bar{v}_L$ at point B provided a value almost indistinguishable from that of the virgin material, once the experimental errors discussed in section ''Ultrasonic method'' are taken in due account; hence, we reported a null estimation of D in Figure 17(e).

Results relevant to sample 50-4 are not reported as well. The ultrasonic technique gave in this case a value of damage unrealistically low, when compared to the relevant micro-tomographic estimation and to the evolution suggested by samples 50-1, 50-2 and 50-3. This underestimation was due to the fact that the size of the adopted probe was too big in comparison with the diameter of the necked cross section of this specimen (see Figure 8(d)), thus providing an unreliable measurement of D. Such issue ought to be carefully considered whenever the ultrasonic wave propagation technique were adopted.

Discussion and conclusions

In this paper, we have presented an experimental assessment of ductile damage in P91 steel tested at high temperature (specifically, at 1100°C) and under quasi-static or high strain rate loading conditions.

To have a picture of damage evolution at increasing elongation of the specimens subject to tensile tests, for each deformation rate a set of tests was conceived at increasing displacement of the testing machine track. Even if not relevant to the same specimen, all the tests in a single set provided overall responses well matching with each other, with a scattering induced only by micromechanical, or metallurgical features; hence, results obtained through a set of tests have been considered as representative of what would happen to a single specimen if it got loaded up to failure.

To assess the overall damage at the end of each test, two methodologies were adopted: micro-tomography, with a synchrotron used as a source of high-intensity X-rays able to penetrate the

cylindrical specimens; ultrasonic measurements of wave speeds in machined samples, obtained from the same specimens previously tested through micro-tomography. While micro-tomography provided images of void distribution in the necking region and a cross sectional measure of damage, data from the ultrasonic apparatus needed to be reduced to directly link the overall damage level under the ultrasonic probe with the shift of the longitudinal wave speed relative to the virgin material. A micromechanical analysis has been therefore given as well, to provide bounds and also a self-consistent estimate on the effect of porosity (in terms of spherical voids dilutely dispersed in a metallic matrix) on the elastic moduli of P91. We have shown that the Poisson's ratio gets marginally affected by the porosity so as, according to a standard assumption in continuum damage mechanics, it can be assumed independent of damage. By assuming instead the Young's modulus to linearly scale with damage, a link between damage and porosity (that, we recall, do have different micromechanical definitions) has been obtained, along with an expression for the speed of longitudinal waves in the damaged region as a function of damage.

Outcomes of micro-tomographic images and of the ultrasonic wave speed shifts have been compared. Even if the presented results are to be considered as preliminary, the two alternative approaches have been shown to agree quite well in all the cases but two. In a first case, the overall damage level in the area under the probe was too low, the shift of the wave speed got comparable with the setup accuracy and the instrumental noise (depending also on the coupling medium between specimen and ultrasonic probe) did not allow to obtain any estimation of the damage level. The other way around, in a second case, the severe necking in the region under the probe produced artifacts, as waves got reflected not only at the rear surface of the specimen but also along its lateral surfaces; hence, the damage was wrongly estimated to be too low in comparison with the other tests. The use of bigger specimens would reduce this effect.

By comparing the two experimental methodologies, it can be stated that micro-tomography provided accurate pictures of the void or damage distribution in each cross section of the specimen, and also a cross sectional measure of its intensity. Ultrasonic measurements provided instead an overall measure of damage, relevant to the whole area of the specimen in contact with the probe. Hence, the resolution of the second methodology looks rather poor, if compared to micro-tomography; nevertheless, it is also to be considered that ultrasonic equipments can be easily used, and their cost is by far smaller than what required to generate high-intensity X-rays with a synchrotron.

Acknowledgements

This paper is published under permission of Mario Rossi, Director of Tenaris Dalmine R&D, who is acknowledged for helpful discussions. The authors wish to thank A. Paggi and E. Palermo of Tenaris Dalmine R&D for their help in the experimental work.

Funding

C. Comi and S. Mariani acknowledge the financial support of Dalmine S.p.A.

Conflict of interest

None declared.

References

Abed F, Al-Tamimi A and Al-Himairee R (2012) Characterization and modeling of ductile damage in structural steel at low and intermediate strain rates. *ASCE Journal of Engineering Mechanics* 138: 1186–1194.

Alves M (2001) Measurement of ductile material damage. *Mechanics Based Design of Structures and Machines* 29: 451–476.

ASTM A335/A335M (2011) Standard specification for seamless ferritic alloy-steel pipe for high-temperature service.

Berthaud Y (1991) Damage measurements in concrete via an ultrasonic technique. Part I experiment. *Cement and Concrete Research* 21: 73–82.

Bonora N, Gentile D, Pirondi A, et al. (2005) Ductile damage evolution under triaxial state of stress: theory and experiments. *International Journal of Plasticity* 21: 981–1007.

Brunig M (2003) An anisotropic ductile damage model based on irreversible thermodynamics. *International Journal of Plasticity* 19: 1679–1713.

Celentano D and Chaboche J-L (2007) Experimental and numerical characterization of damage evolution in steels. *International Journal of Plasticity* 23: 1739–1762.

Comi C, Fedele R and Perego U (2009) A chemo-thermo-damage model for the analysis of concrete dams affected by alkali-silica reaction. *Mechanics of Materials* 41: 210–230.

Hansen T (1965) Influence of aggregate and voids on modulus of elasticity of concrete, cement mortar, and cement paste. *Journal of the American Concrete Institute* 62: 193–216.

Heukamp F, Ulm F-J and Germaine J (2001) Mechanical properties of calcium leached cement pastes: triaxial stress states and the influence of the pore pressure. *Cement and Concrete Research* 31: 767–774.

Kendall K, Howard A and Birchall J (1983) The relation between porosity, microstructure and strength, and the approach to advanced cement-based materials. *Philosophical Transactions of the Royal Society of London A: Mathematical, Physical and Engineering Sciences* 310: 139–153.

Lemaitre J (1985a) A continuous damage mechanics model for ductile fracture. *Journal of Engineering Materials and Technology* 107: 83–89.

Lemaitre J (1985b) Coupled elasto plasticity and damage constitutive equations. *Computer Methods in Applied Mechanics and Engineering* 51: 31–49.

Lemaitre J and Dufailly J (1987) Damage measurements. *Engineering Fracture Mechanics* 28: 643–661.

Li S and Wang G (2008) *Introduction to micromechanics and nanomechanics*. Singapore: World Scientific.

Nadal M-H, Hubert C and Oltra R (2009) High temperature shear modulus determination using a laser-ultrasonic surface acoustic-wave device. *Journal of Applied Physics* 106: 024906.

Needleman A and Tvergaard V (1984) An analysis of ductile rupture in notched bars. *Journal of the Mechanics and Physics of Solids* 32: 461–490.

Nemat-Nasser S and Hori M (1993) Micromechanics: overall properties of heterogeneous materials. In: Achenbach JD, Budiansky B, Lauwerier HA, et al. (eds) *Applied Mathematics and Mechanics*. Vol. 37. Amsterdam: North Holland.

Ohtsu M (2011) Damage evaluation in freezing and thawing test of concrete by elastic-wave methods. *Materials and Structures* 44: 1725–1734.

Saanouni K and Chaboche J (2003) Computational damage mechanics: Application to metal forming simulation. In: Milne I, Ritchie R and Karihaloo B (eds) *Comprehensive structural integrity* (Vol. 3, chapter 6). Elsevier Science, pp. 321–376.

Saanouni K, Forster C and Ben Hatira F (1994) On the inelastic flow with damage. *International Journal of Damage Mechanics* 3: 140–169.

Spitzig W, Smelser R and Richmond O (1988) The evolution of damage and fracture in iron compacts with various initial porosities. *Acta Metallurgica* 36: 1201–1211.

Thuillier S, Maire E and Brunet M (2012) Ductile damage in aluminium alloy thin sheets: correlation between micro-tomography observations and mechanical modeling. *Materials Science and Engineering A* 558: 217–225.

Tinet H, Klocker H and Le Coze J (2004) Damage analysis during hot deformation of a resulfurised stainless steel. *Acta Materialia* 52: 3825–3842.